**Title:** CIT tumor lines: A novel series of immunogenic squamous cell skin carcinoma cell lines derived from chemical carcinogenesis

**Authors**

Miho Tanaka[1,*], Robert Letchworth[2,3,*], Alina A Barnes[2,3], Lotus Lum[1], Savannah Hughes[2], Grant Schlauderaff[2], Piyush Chaudhary[2,3], Kenneth M Ng[1], Daphne Superville[1], Corinna Martinez Luna[1], Maria Gonzalez[1], Allie Grossmann[4], Melissa Q Reeves[2,3]

**Affiliations**

[1]Department of Microbiology and Immunology, University of California, San Francisco

[2]Huntsman Cancer Institute, University of Utah

[3]Department of Pathology, University of Utah

[4]Earle A. Chiles Research Institute, Providence Cancer Institute of Oregon, Portland, OR

[*]These authors contributed equally.

Correspondence: melissa.reeves@hci.utah.edu

**Keywords**

Squamous cell skin carcinoma, tumor immunology, tumor neoantigen, immune checkpoint inhibitor, mouse models of cancer

**Abstract**

Immunotherapy is now widely used to treat cancer, but its efficacy in many cancer types remains modest. To overcome current barriers, preclinical mouse models that faithfully recapitulate the diversity of cancer types, tumor genetics, mutation burdens, and neoantigen patterns of human tumors are essential. Currently, there are relatively few transplantable murine models of squamous cell carcinomas (SCC). Here we describe a novel series of 11 skin SCC tumor lines, the Carcinogen-Induced Tumor (CIT) lines, syngeneic to the FVB strain. The CIT lines were established from skin carcinomas induced by DMBA and TPA treatment, and harbor genetic drivers and overall tumor mutational burdens that recapitulate those found across multiple human SCCs. Each CIT line gives rise to tumors with a consistent immune infiltration pattern, ranging from T cell-rich "hot" tumors to T cell-poor "cold" tumors. Hot CIT lines exhibit partial responses to treatment with immune checkpoint inhibitors, and we have identified two neoantigens present in an immunotherapy-responsive CIT line. The CIT lines thus provide a valuable new series of preclinical models for studying anti-tumor immune responses and developing strategies to improve immunotherapy efficacy in SCCs.

## Introduction

Over the past decade, immunotherapy has become a new pillar of cancer treatment[1,2]. While immunotherapy holds immense potential to cure even advanced disease, this promise has only been realized in a handful of cancer types[1]. Murine models play a vital role in basic and translational cancer research, providing a means of conducting mechanistic experiments to dissect cancer and immune cell biology and their interactions with therapy. Transplantable

45 tumor models, in which cancer cell lines are implanted into immunocompetent syngeneic hosts,
46 play a particularly important role in preclinical research, as the reliability of their growth
47 kinetics makes them a workhorse for testing the efficacy of new therapies or combinations.
48 However, a large proportion of murine tumor immunology studies to date have relied on a
49 small number of widely-used transplantable tumor models, such as MC38 colorectal cancer and
50 B16 melanoma. Recent years have also seen a rise in the use of genetically engineered mouse
51 models (GEMMs) of lung adenocarcinoma[3–6], pancreatic cancer[7,8], and melanoma[9] in
52 immunotherapy studies.

53 However, there remain significant gaps in mouse models for studying the anti-tumor
54 immune response. Many barriers to the efficacy of immunotherapy are cancer type-specific,
55 and there is a need for mouse models that accurately recapitulate the unique features of each
56 disease. Additionally, the majority of mouse models currently used for immunotherapy studies
57 are syngeneic to C57BL/6 mice, which are known to have a Th1-biased immune response[10].
58 While this is likely beneficial for tumor control—and C57BL/6 mice are widely known for their
59 resistance to tumorigenesis[11,12]—it is not necessarily representative of the diversity of human
60 immune responses. While no single mouse model or mouse strain can represent the full
61 spectrum of human immunity, increasing the diversity of mouse strains used to model anti-
62 tumor immune responses is essential to capture human diversity.

63 Here we describe the Carcinogen-Induced Tumor (CIT) cell line panel, a novel series of
64 murine squamous cell skin carcinoma (skin SCC) cell lines that help to address many of these
65 gaps. Skin SCC is one of the most common cancer types in the United States[13,14]. While early
66 stage disease is frequently curable by surgery, immune checkpoint inhibitors (ICIs) including

67 anti-PD-1 are FDA-approved for patients who have locally advanced, recurrent or metastatic
68 skin SCC[15]. ICI treatment of skin SCC patients yields response rates of 50% in locally advanced
69 disease[16,17] and drops as low as 35% in metastatic disease[16]. While this makes skin SCC a
70 disease type that is considered to respond well to ICIs, there is nonetheless a substantial
71 proportion of patients with advanced skin SCC who currently do not benefit from
72 immunotherapy. Additionally, SCCs at other anatomical sites—which share similar genetic
73 drivers to skin SCC[13,18–20]—exhibit even more limited responses to ICI, with head and neck SCC
74 patients exhibiting a 15-18% response rate[21,22], and esophageal SCC patients exhibiting 14-28%
75 response rates[23].
76 SCCs are highly underrepresented among murine models of cancer and have few cell
77 line models available, with the MOC series of three oral SCC lines[24] being the main SCC models
78 to be widely used. To address this gap, we have established the CIT cell lines. The CIT lines are
79 derived from DMBA/TPA-induced skin SCCs, and they are syngeneic to the FVB strain, which—in
80 contrast to C57BL/6—is known to exhibit Th2-biased immune responses[10,25] and to be readily
81 susceptible to tumorigenesis. The CIT cell lines recapitulate both the mutational profiles and
82 antigen burdens of human SCCs. Although all the CIT lines are derived from skin SCCs, they
83 harbor alterations in driver genes that are relevant to many SCC types, including *Hras* and
84 *Trp53*. This is consistent with our previous work showing DMBA/TPA-induced murine skin SCCs
85 are driven by the same genetic programs as human lung, head and neck, and esophageal
86 SCCs[26]. As a result of being chemically induced in immune-competent hosts, the CIT lines
87 further carry endogenous neoantigens that have survived immune selection during tumor
88 progression of the original carcinoma. Furthermore, tumors arising from the CIT lines exhibit a

89 range of reproducible patterns of immune infiltration—from high to low T cell infiltrate—along
90 with a corresponding range of responses to immunotherapy.
91 The CIT cell line series thus offers a panel of SCC tumor models that exhibit a range of
92 mutational burdens, immune infiltrates, and neoantigen expression, while being driven by SCC-
93 relevant genomic drivers and exhibiting histopathologic features characteristic of SCCs. These
94 properties make the CIT lines a valuable set of preclinical models for investigating tumor
95 biology and responses to therapy, particularly immunotherapy, in SCCs.
96
97 **Results**
98
99 **CIT lines display a range of reproducible immune infiltration phenotypes.**
100 The CIT cell lines were derived from skin carcinomas that arose by topically treating *K5-*
101 *CreERT2-Confetti* FVB/N mice with a single dose of 7,12-dimethylbenzanthracene (DMBA)
102 followed by 12-O-tetradecanoylphorbol-13-acetate (TPA) twice weekly for 20 weeks, using a
103 well-established skin carcinogenesis protocol[27,28] (**Fig. 1A**). In the DMBA/TPA model, benign
104 papillomas arise after about 6 weeks of TPA treatment, and approximately 10% of these
105 progress to malignant carcinomas. Primary carcinomas were resected when they were
106 approximately 1cm in longest diameter, digested into a single cell suspension, and grown under
107 standard tissue culture conditions (DMEM with 10% FBS, antibiotics, and antimycotics). Each
108 cell line was established in tissue culture for >10 passages. Implantation of $1.25 \times 10^5$ tumor cells
109 into the subcutaneous flank of FVB mice gave rise to tumors with 100% penetrance, and we
110 subsequently profiled the histopathologic and immune characteristics of these tumors.

111 We carried out immune profiling of 11 CIT cell lines by flow cytometry, quantifying the
112 number of total T cells, CD4+ and CD8+ T cells in tumors from each CIT model **(Supp. Fig. 1A)**.
113 We found each CIT line gave rise to tumors with a consistent pattern of immune infiltration,
114 spanning the range of immune hot (highly infiltrated by T cells, e.g., CIT18) to immune cold
115 (poorly infiltrated by T cells, e.g., CIT9) (**Fig. 1B**). Interestingly, we observed a consistent bias in
116 the T cell compartment toward CD4+ T cells, about half of which were Tregs **(Supp. Fig. 1B)**. We
117 selected 5 CIT lines, including representation of both hot and cold models, for more extensive
118 immune profiling **(Supp. Fig. 1A)**. On the whole, we found the myeloid compartment of CIT
119 tumors was strongly biased toward macrophages (CD11b+MHCII+F4/80+), with relatively fewer
120 Ly6C+ and Ly6G+ myeloid cells (monocytes and neutrophils, respectively) (**Fig. 1C**). Macrophage
121 infiltration was highest in the two coldest (lowest T cell infiltrate) CIT models, CIT22 and CIT9.
122 Conversely, hot models CIT18 and CIT6 exhibited the highest B cell infiltration (**Fig. 1C**). There
123 was no clear trend between hot and cold tumors for $Ly6G^{hi}Ly6C^{mid}$ neutrophils, $Ly6C^{hi}$CD11b+
124 monocytes, or CD11c+MHCII+ dendritic cells.
125 Tumor histology for the same five selected CIT tumor models was reviewed by a board-
126 certified pathologist. Tumors from all CIT models were poorly differentiated, spindled, arranged
127 in fascicles, and highly mitotic (**Fig. 1D**). Some CIT18 tumors contained pleomorphic, rhabdoid,
128 or epithelioid malignant cell morphologies. Among the hot models, CIT18 and CIT17 tumors
129 contained brisk tumor-infiltrating lymphocyte (TIL) infiltration, while CIT6 tumors contained
130 focal clusters of TILs or TILs localized to the edge of the tumor. In comparison, tumors arising
131 from the cold lines CIT9 and CIT22 displayed very little TIL infiltration. CIT6, CIT17, CIT18 and
132 CIT22 tumors contained diffuse infiltration of polymorphonuclear (PMN) cells, while PMNs in

133 cold CIT9 tumors were largely restricted to the edge of the tumors. Altogether, we find that the
134 CIT cell lines give rise to tumors that recapitulate the histologic features of high grade,
135 sarcomatoid SCC, and each exhibit characteristic patterns of immune infiltration.
136
137 **Genomic profiles of CIT lines recapitulate human SCC.**
138 All 11 CIT cell lines were subjected to exome sequencing, to a median depth of 153X.
139 Consistent with previous sequencing of DMBA/TPA tumors by ourselves and others[26,29,30], CIT
140 cell lines were genomically characterized by *Hras* driver mutations, a substantial mutation
141 burden, and whole-chromosome copy number alterations. The mutation burden among the CIT
142 lines ranged from 46 to 256 non-synonymous mutations (**Fig. 2A, Table 1**). Ten of our CIT lines
143 exhibited an *Hras* Q61L mutation, while one, CIT16, exhibited an *Hras* G12V as well as a *Kras*
144 G13R mutation (**Fig. 2B**). Seven CIT lines displayed additional non-synonymous mutations in
145 driver genes known to be mutated in human cutaneous, head and neck, lung, and esophageal
146 SCC, including *Trp53* and *Fgfr3*. (**Fig. 2B**). The majority of total mutations were T>A
147 transversions, with a particular prevalence of CTN>A mutations (with N representing any
148 nucleotide) consistent with the known mutagenic signature of DMBA[26,29,30] **(Fig. 2C)**. The CIT
149 lines also harbored whole-chromosome alterations, primarily amplifications, especially on
150 chromosomes 6 and 15 **(Fig. 2D)**. Chromosome 6 amplifications are common in DMBA/TPA
151 carcinomas[26]. Chromosome 15 amplifications were also previously observed, but they were
152 more heavily represented in the CIT lines than in a previously sequenced cohort of primary
153 tumors[26], suggesting perhaps a selection in cell culture for lines with this amplification.
154 Interestingly, we saw no whole-chromosome amplifications of chromosome 1 and only one

155 amplification of chromosome 7. We previously reported that chromosome 1 and 7
156 amplifications are common in DMBA/TPA carcinomas with an epithelial-like "squamous"
157 morphology, but largely absent in DMBA/TPA carcinomas with a mesenchymal-like "spindle"
158 morphology [26]. The underrepresentation of these alterations is perhaps not surprising given
159 that the CIT lines primarily give rise to tumors with spindle cell morphology, but may again
160 suggest a selection bias of the cell lines we were able to establish in culture.
161 Given that mutation burden information and immune phenotypes were available for all
162 11 cell lines, we examined whether a relationship existed between these metrics. While two of
163 the tumors with the highest T cell infiltration, CIT18 and CIT6, exhibited two of the three
164 highest mutation burdens, we observed that tumor model with the second-highest T cell
165 infiltration, CIT16, had a relatively low mutation burden. CIT23 tumors, which had the second-
166 highest mutation burden, were by contrast very poorly infiltrated by T cells (**Fig. 1B, 2A**). Thus,
167 aligning with observations from patients, mutation burden alone was insufficient to predict the
168 immune response to any given tumor.
169
170 **Immunologically hot CIT lines respond to immunotherapy.**
171 Because our CIT lines exhibited moderate to high tumor mutation burdens, we
172 hypothesized they would carry neoantigens and would be sensitive to immune checkpoint
173 inhibitors (ICIs). We tested the efficacy of a combination ICI regimen—anti-PD-1 plus anti-CTLA-
174 4, administered as two doses 3 days apart—on CIT18, CIT6, and CIT9 tumors (**Fig. 3A**).
175 CIT18 and CIT6 tumors—both of which we had observed to be immunologically hot—
176 grew significantly slower than controls when treated with anti-PD-1 plus anti-CTLA-4 (hereafter,

177 “ICI”) **(Fig. 3B)**. Conversely, immunologically cold CIT9 tumors displayed no difference in growth
178 between ICI-treated and control tumors **(Fig. 3B)**. We carried out immune profiling of ICI- and
179 control-treated tumors to interrogate how ICI remodeled the immune response in these
180 models. CIT18 tumors had the strongest response to ICIs, both in terms of the reduction in
181 growth and in the increase in tumor infiltrating T cells. Total T cells, CD8+ T cells and CD4+ T
182 cells were all more abundant in ICI-treated CIT18 tumors (**Fig. 3C**, **Supp. Fig. 2A**). CIT6 tumors,
183 which also showed a response to ICI, only exhibited an influx of CD8+ T cells following ICI, while
184 CIT9 tumors showed no increase in overall T cell infiltration. **(Fig. 3D-E**, **Supp. Fig. 2A)**.
185 ICI treatment also altered the activation profile of tumor-infiltrating T cells. Effective ICI
186 treatment in CIT18 and CIT6 tumors was accompanied by an increase in the percentage of CD8+
187 and CD4+ T cells which exhibited a CD44+CD62L- “effector-like” phenotype **(Fig. 3F-G**, **Supp.**
188 **Fig. 2B).** Notably, in hot tumors this increase in “effector-like” CD8+ T cells resulted in a skewing
189 of the CD8+ compartment away from a CD44+CD62L+ “central memory-like” phenotype, even
190 though the abundance of central memory-like CD8+ T cells as a percent of all immune cells was
191 unchanged **(Supp. Fig. 2C)**. In contrast, ICI treatment in cold CIT9 tumors was unsuccessful at
192 shifting the phenotype of either CD8+ or CD4+ T cells **(Fig. 3H**, **Supp. Fig. 2B-C)**. We further
193 examined the expression of PD-1, which is present on both activated and exhausted T cells, and
194 Tim3 and TIGIT, both of which mark exhaustion, in CD8+ T cells. The proportion of tumor-
195 infiltrating CD8+ T cells expressing PD-1 increased after ICI treatment in all three tumor models
196 **(Fig. 3I-K)**. Interestingly, the “activated” PD-1+Tim3-TIGIT- T cell population was the primary
197 CD8+ population to increase in CIT18 tumors following ICI, and this corresponded to the best
198 tumor growth control **(Fig. 3I, Supp. Fig. 2D)**. By contrast in CIT6 tumors, which showed more

199 modest tumor growth control, the proportion of "activated" PD-1+Tim3-TIGIT- CD8+ T cells did
200 not increased as a fraction of PD-1+ CD8+ T cells **(Fig. 3J)**. Instead, there was an increase in the
201 proportion of PD-1+ CD8+ T cells with an exhausted (PD-1+Tim3+ or PD-1+Tim3+TIGIT+)
202 phenotype after ICI treatment **(Supp. Fig. 2D)**. Together, this data shows that CIT tumor models
203 exhibit a range of responses to immunotherapy, and that the degree of sensitivity appears to
204 be approximately correlated with the level of T cell infiltration in untreated tumors.
205
206 **CIT tumors display identifiable and immunotherapy-sensitive neoantigens.**
207 Given that improvement in the CD8+ T cell response corresponded to effective tumor
208 control following ICI, we next sought to identify the neoantigens recognized during this
209 response. We focused here on the CIT6 tumor model, which exhibited the intermediate
210 response to ICI among the three models tested and thus may be most representative of patient
211 tumors which are recognized by the host immune response but benefit only marginally from
212 current ICI strategies. We employed the NetH2pan algorithm[31] to predict the binding strength
213 between the H2-Dq and H2-Kq MHCI alleles carried by FVB/N mice and the neoepitopes
214 predicted to be generated by all non-synonymous mutations identified in our exome
215 sequencing analysis. We identified 27 top binders, and these were further filtered to prioritize
216 those for which the mutant sequence was predicted to exhibit better binding than the wild-
217 type sequence, and for which we could detect expression of the gene by RNAseq (**Fig. 4A-B**,
218 **Table 2)**.
219 Candidate neoantigens identified through this pipeline were subsequently screened by
220 *in vitro* IFNγ ELISPOT assay[32,33]. Whole splenocytes, CD8+ T cells, or CD4+ T cells from the spleen

221 of CIT6 tumor-bearing mice were incubated with synthetic peptides corresponding to each
222 candidate epitope sequence (**Fig. 4C**). We identified two peptides, CPAFLPCTV (resulting from a
223 Brinp3 T436P mutation) and VPPSSLLPL (resulting from a Ttll4 Q454L mutation), which
224 consistently elicited IFNγ production in sorted CD8+ T cells from CIT6-bearing mice in a peptide
225 concentration-dependent manner (**Fig. 4D-G**). These peptides elicited no response from sorted
226 CD4+ T cells (**Supp. Fig. 3A**). When the peptide assay was carried out with whole splenocytes
227 (no prior sorting of CD8+ or CD4+ T cells), the dose-dependent response to VPPSSLLPL (Ttll4
228 Q454L mutation) was still observed, but the response to CPAFLPCTV (Brinp3 T436P mutation)
229 was not detectable above background (**Supp. Fig. 3B**).
230 We next interrogated the effect of ICI therapy on the T cell response to VPPSSLLPL,
231 focusing on VPPSSLLPL because its response was more clearly detected in whole splenocytes
232 **(Supp. Fig. 3B)**. CIT6 tumors were treated with three doses of anti-PD-1 and anti-CTLA-4
233 combination therapy (**Fig. 4H**), and an IFNγ ELISPOT assay was carried out on whole splenocytes
234 harvested 3 days after the final dose of ICI. Splenocytes from ICI-treated mice produced a
235 robust IFNγ response when incubated with VPPSSLLPL compared to no peptide **(Fig. 4I)**,
236 indicating that response to the neoantigen VPPSSLLPL is prominent during immunotherapy
237 response.
238
239 **Discussion**
240 We have established the CIT lines as a novel series of *Hras*-driven skin SCC tumor lines, and
241 here present comprehensive histologic, genomic, and immune characterization of these 11 cell
242 lines. The CIT lines carry genomic drivers relevant to human SCC, as well as a moderate-to-high

243 mutation burden[13,18,19]. We show that each CIT line exhibits a characteristic immune infiltrate,
244 with individual cell lines ranging from immune hot to immune cold. Immune hot CIT lines CIT6
245 and CIT18 exhibit partial responses to an immunotherapy regimen of anti-CTLA-4 and anti-PD-1.
246 We have also identified two neoantigens that elicit CD8+ T cell responses in the CIT6 cell line. Of
247 note, while numerous neoantigens have been identified in tumor models syngeneic to
248 C57BL/6[6,32–35], there has been a notable dearth of neoantigen identification in other mouse
249 strains including FVB. Antigen identification efforts in FVB mice to date have largely focused on
250 breast cancer models and identification of antigens arising from the MMTV-PyMT construct or
251 identification of tumor-associated antigens, rather than neoantigens arising from tumor
252 mutations[36]. The CIT lines, with the identification of two MHCI-restricted neoantigens in CIT6,
253 thus provide a valuable new series of models for immunotherapy research in squamous cell
254 carcinoma.

255 An additional feature of the CIT lines, having been derived from *K5CreERT2-Confetti*
256 mice, is that cells can be labeled with fluorescent tags following exposure to Cre
257 recombinase[28,37]. We have successfully labeled CIT lines *in vitro* using adenoviral Cre
258 recombinase. While the *K5CreERT2* allele will also allow for labeling of K5+ cells following
259 tamoxifen treatment, we have found low expression of K5 in these cell lines—as well as in
260 DMBA/TPA tumors following progression to the carcinoma stage[28] —making this approach less
261 effective. Introducing Cre and subsequently sorting cells enables the establishment of isogenic
262 cell lines with each GFP, YFP, RFP or CFP[37]; while introducing Cre to activate labeling without
263 sorting could allow for multiclonal lineage tracing.

264 Improving immunotherapy outcomes in SCC remains an unmet clinical need. The CIT
265 panel of SCC tumor lines provides an important new set of tools to better understand the
266 mechanisms behind immunotherapy resistance in SCC, and to preclinically model novel
267 approaches to overcoming ICI resistance and improving SCC patient outcomes.
268
269 **Materials and methods:**
270 Carcinogenesis and cell line generation
271 To induce tumors, *K5CreER-Confetti FVB/N* mice were treated with 25 µg DMBA followed by
272 TPA (200 µl of a $10^{-4}$ M solution in acetone) two times a week for 20 weeks. To generate cell
273 lines, carcinomas were resected at a size of >1 cm in longest diameter, finely chopped, digested
274 in DMEM containing Collagenase I and IV and DNase I for 45 minutes at 37 °C, washed with PBS,
275 plated in DMEM plus 10% heat-inactivated FBS and L-glutamine, with penicillin, streptomycin,
276 and amphotericin B, and passaged until cells stably grew in culture.
277
278 In vivo experiments and immune checkpoint inhibitor treatment
279 A total of $1.25 \times 10^5$ cells were injected subcutaneously into the dorsal flank of 8 to 16 week old
280 male and female FVB/N mice. For baseline flow cytometric immune profiling and histological
281 analysis (Fig. 1), tumors were harvested approximately 21 days post-engraftment, when tumors
282 measured ~1cm in diameter. For immune checkpoint inhibitor (ICI) experiments (Fig. 3), mice
283 were enrolled in treatment 14 days post-tumor engraftement, when tumors grew to 25-100
284 $mm^3$ in volume. Mice were treated with 200 µg anti-PD-1 (BioXCell Catalog# BE0146) and 200
285 µg anti-CTLA-4 (BioXCell Catalog# BE0131) or 200 µg isotype control (BioXCell Catalog#

286 BE0089). Mice received two doses 3 days apart. Mice were harvested when tumors were
287 ~10mm in length, typically 17-21 days post-ICI enrollment and 31-35 days post-tumor
288 engraftment, or when an ethical endpoint was reached. All animal experiments were approved
289 by the by the University of Utah Office of Comparative Medicine (IACUC #22-02003) or by the
290 University of California San Francisco Laboratory Animal Resource Center (IACUC #AN187679).
291 This work complies with all the relevant ethical regulations regarding animal research.
292
293 Flow cytometric immune profiling
294 Harvested tumors were finely chopped, digested in DMEM containing Collagenase IV (Sigma-
295 Aldrich Catalog# 9001-12-1) and DNase I (Sigma-Aldrich Catalog# D5025-15KU) for 45 minutes
296 at 37 °C, and filtered through 70um filters. Cells were counted using a Countess III, and 5 million
297 cells were plated and stained with antibodies and Live/Dead NIR stain. Antibodies used for flow
298 cytometric analyses are listed in **Table 1**. Flow cytometry analysis was performed on a Cytek
299 Aurora.
300
301 Histology
302 Harvested tumors were fixed in formalin for 24 hours, placed in cassettes (VWR Catalog#
303 18000), submerged in 70% ethanol, and submitted to ARUP Laboratories Research Histology
304 Core Laboratory, where they were embedded in paraffin, cut into 4µm-thick slices, stained with
305 hematoxylin and eosin (H&E) and mounted on slides. The 4µm slides were then analyzed by a
306 board-certified pathologist, A.G..
307

308 Cell line sequencing

309 DNA was extracted from cultured cells from each cell line and from tails of the mice in which
310 each tumor originated using the Qiagen DNeasy Blood & Tissue DNA purification kit (Qiagen).
311 Whole exome sequencing was performed using the Agilent Sure Select Mouse Exon capture kit,
312 and sequenced to an average depth of 153X on an Illumina HiSeq X by MedGenome, Inc. in
313 Redwood City, CA. Reads were trimmed with cutadapt (v3.5)[38] and aligned to the mm10 mouse
314 genome using BWA (v0.7.17)[39]. Reads were deduplicated using MarkDuplicates and
315 recalibrated using BaseRecalibrator from GATK (v4.1)[40]. Mutations were called using MuTect2
316 (GATK v4.1)[40,41] and Strelka2 (v2.9.10)[42], using tails from the mice in which each tumor
317 developed as the matched normal. Mutation calls were filtered using the following criteria:
318 minimum read depth of 10 at the mutation position in both tumor and normal samples;
319 minimum of 4 reads supporting the mutation call; for Strelka only, minimum quality QSS score
320 of 25. Mutations that passed all filters with both callers were kept and were additionally filtered
321 to remove any germline SNP detected in the panel of normals. Final mutation calls were
322 annotated with Annovar[43]. Copy number calling was performed with CNVkit[44], using all tails as a
323 pooled normal. Exome sequencing data from CIT lines is available in SRA (accession number
324 PRJNA1129114).

325

326 Neoantigen peptide prediction

327 Mutations identified by exome sequencing were used to construct wild-type and mutant amino
328 acid sequences of all 7mer, 8mer, and 9mer peptides that included each identified single
329 nucleotide variant. The NetH2pan algorithm was used to predict binding affinity and percentile

330 rank for each wild-type and mutant peptide sequence. This data was filtered using the following
331 criteria: mutant peptide with a percentile rank <0.5, log affinity ratio >0 (affinity ratio defined as
332 ratio of predicted binding affinity of mutant sequence dividesd by wild-type sequence), and a
333 gene expression >300 RPM based on RNAseq of whole CIT6 and CIT9 tumors.
334
335 ELISpot assays
336 Whole spleens were harvested from FVB mice and processed by crushing through a 70µm mesh
337 filter, pre-wet with 1X PBS, using a syringe plunger and washed. Red blood cells were lysed for 5
338 minutes using ACK lysis buffer and splenocytes counted. Spleens from CIT6-bearing FVB mice
339 were harvested 2-4 weeks after tumor inoculation. CD8+ T cells were isolated from whole
340 spleens using EasySep™ Mouse CD8+ T Cell Isolation Kits (STEMCELL Technologies Catalog#
341 19853) and CD4+ T cells were isolated from whole spleens using EasySep™ Mouse CD4+ T Cell
342 Isolation (STEMCELL Technologies Catalog# 19852).
343 Interferon-gamma (IFNγ) ELISpots were performed over a three-day assay.
344 Multiscreen®HTS 96-well filtration plate(s) were coated with IFNγ capture antibody (clone AN-
345 18, Catalog# 517902), diluted 1:500 in 1X PBS. Plates were wrapped in aluminum foil to equally
346 distribute temperature and incubated overnight, or at least 18 hours, at 4°C. The following day
347 plates were washed twice with 200µl RPMI-2 (RPMI with 2% FBS, 1% L-glutamate, 1%
348 streptococcus and penicillin antibiotic solution, and 0.09% 2-Mercaptoethanol (BME)) and
349 blocked for two hours with 200µl of RPMI-20 (RPMI with 20% FBS, 1% L-glutamate, 1%
350 streptococcus and penicillin antibiotic solution, and 0.09% 2-Mercaptoethanol (BME)) before
351 splenocytes or T cells were added. For assays where total splenocytes were used, 500,000

352 splenocytes were plated per well. For assays using CD8+ and CD4+ T cells, 20,000 cells per well
353 were co-cultured with 500,000 splenocytes from a non-tumor-bearing mouse to provide a
354 source of antigen presenting cells. Stimulation medium was prepared by diluting synthetic
355 peptide in RPMI-10 to desired peptide concentration(s). All synthetic peptides used for these
356 assays were ordered through GenScript. Peptides were reconstituted in DMSO or MilliQ water
357 according to solubility testing provided by the manufacturer. Reconstituted peptides were
358 aliquoted and frozen at -80°C. The negative control consisted of MilliQ water and RPMI-10.
359 Positive control contained 0.04% Phorbol 12-myristate 13-acetate (PMA) and 0.09% Ionomycin
360 in RPMI-10.
361 Plates were wrapped in aluminum foil and incubated undisturbed at 37°C and 5% CO2
362 for 44-48 hours before developing using biotinylated anti-IFNγ detection antibody (clone R4-
363 6A2, Catalog# 505704), streptavidin-HRP enzyme conjugation (Thermofisher, Catalog# 405210),
364 and AEC (3-amino-9-ethyl-carbazole) substrate. AEC substrate was prepared by dissolving 20
365 mg of AEC in 2 ml of N, N Dimethylforamamide (Sigma-Aldrich, Catalog# 227056), diluting in 0.1
366 M Acetate Solution, adding hydrogen peroxide and filtering with a 0.45µM filter. Spots were
367 Imaged using the Agilent BioTek Cytation7 and analyzed using the Gen5 software.
368
369 **Data availability**
370 Exome sequencing of CIT lines is available in SRA (accession number PRJNA1129114).
371
372 **Acknowledgements**

373 This work was supported by the UCSF Program for Breakthrough Biomedical Research (PBBR)
374 Sandler Fellowship, US National Cancer Institute (NCI) grant R21CA264599, the Huntsman
375 Cancer Institute Cancer Center Support Grant P30CA040214, the American Cancer Society IRG-
376 21-131-01, Five For The Fight, The Cancer League, and the V Foundation (V2024-002). G.S. is
377 supported by the Institute of General Medical Sciences grant T32GM141848. We thank the
378 University of Utah Flow Cytometry Core, the Associated Regional and University Pathologists,
379 Inc. (ARUP Laboratories) Research Histology Core, the University of Utah Center for High
380 Performance Computing (CHPC), and the Preclinical Research Resource (PRR), in particular D.
381 Lum and W. Sun, and the UCSF Parnassus Flow CoLab. We also thank A. Lai for help establishing
382 the ELISPOT methods. The computational resources used for exome sequencing analysis were
383 partially funded by the NIH Shared Instrumentation Grant 1S10OD021644-01A1. We thank and
384 all members of the Reeves Lab for thoughtful input during the development of this story. Some
385 figures were created with Biorender.com.
386

387 **Author contributions**

388 M.T., R.L., L.L., A.B., and M.Q.R. designed the project and experiments. R.L., S.H., M.T., L.L. and
389 M.Q.R. led experiment implementation and data analysis. A.B. designed and carried out the
390 neoantigen identification experiments. S.H. and G.S. carried out the immune checkpoint
391 inhibitor experiments, with support from R.L. Board-certified pathologist A.G. provided
392 histology review. R.L., M.T. and M.Q.R. wrote the manuscript, with input from other co-authors.
393 P.C., K.N., D.S., C.M.L. and M.G. assisted with experiments.
394

395 **References**

396


397 1. Ribas, A. & Wolchok, J. D. Cancer immunotherapy using checkpoint blockade. *Science*
398 **359**, 1350–1355 (2018).
399 2. Chen, D. S. & Mellman, I. Elements of cancer immunity and the cancer-immune set point.
400 *Nature* **541**, 321–330 (2017).
401 3. Schenkel, J. M. *et al.* Conventional type I dendritic cells maintain a reservoir of
402 proliferative tumor-antigen specific TCF-1+ CD8+ T cells in tumor-draining lymph nodes.
403 *Immunity* **54**, 2338-2353.e6 (2021).
404 4. Burger, M. L. *et al.* Antigen dominance hierarchies shape TCF1+ progenitor CD8 T cell
405 phenotypes in tumors. *Cell* **184**, 4996-5014.e26 (2021).
406 5. Nguyen, K. B. *et al.* Decoupled neoantigen cross-presentation by dendritic cells limits
407 anti-tumor immunity against tumors with heterogeneous neoantigen expression. *Elife*
408 **12**, e85263 (2023).
409 6. Roerden, M. *et al.* Neoantigen architectures define immunogenicity and drive immune
410 evasion of tumors with heterogenous neoantigen expression. *J Immunother Cancer* **12**,
411 e010249 (2024).
412 7. Li, J. *et al.* Tumor Cell-Intrinsic Factors Underlie Heterogeneity of Immune Cell Infiltration
413 and Response to Immunotherapy. *Immunity* **49**, 178-193.e7 (2018).
414 8. Byrne, K. T. & Vonderheide, R. H. CD40 Stimulation Obviates Innate Sensors and Drives T
415 Cell Immunity in Cancer. *Cell Rep* **15**, 2719–2732 (2016).

416 9. Wee, Y. *et al.* Tumour-intrinsic endomembrane trafficking by ARF6 shapes an
417 immunosuppressive microenvironment that drives melanomagenesis and response to
418 checkpoint blockade therapy. *Nat Commun* **15**, 6613 (2024).
419 10. Sellers, R. S., Clifford, C. B., Treuting, P. M. & Brayton, C. Immunological variation
420 between inbred laboratory mouse strains: Points to consider in phenotyping genetically
421 immunomodified mice. *Vet Pathol* **49**, 32–43 (2012).
422 11. Hennings, H., Shores, R., Mitchell, P., Spangler, E. F. & Yuspa, S. H. Induction of
423 papillomas with a high probability of conversion to malignancy. *Carcinogenesis* **6**, 1607–
424 10 (1985).
425 12. Davie, S. A. *et al.* Effects of FVB/NJ and C57Bl/6J strain backgrounds on mammary tumor
426 phenotype in inducible nitric oxide synthase deficient mice. *Transgenic Res* **16**, 193–201
427 (2007).
428 13. Chang, D. & Shain, A. H. The landscape of driver mutations in cutaneous squamous cell
429 carcinoma. *NPJ Genom Med* **6**, 61 (2021).
430 14. Nehal, K. S. & Bichakjian, C. K. Update on Keratinocyte Carcinomas. *New England Journal*
431 *of Medicine* **379**, 363–374 (2018).
432 15. Ansary, T. M., Hossain, M. R., Komine, M. & Ohtsuki, M. Immunotherapy for the
433 Treatment of Squamous Cell Carcinoma: Potential Benefits and Challenges. *International*
434 *Journal of Molecular Sciences* **23**, 8530 (2022).
435 16. Hughes, B. G. M. *et al.* Pembrolizumab for locally advanced and recurrent/metastatic
436 cutaneous squamous cell carcinoma (KEYNOTE-629 study): an open-label,
437 nonrandomized, multicenter, phase II trial. *Annals of Oncology* **32**, 1276–1285 (2021).

438 17. Migden, M. R. *et al.* PD-1 Blockade with Cemiplimab in Advanced Cutaneous Squamous-
439 Cell Carcinoma. *New England Journal of Medicine* **379**, 341–351 (2018).
440 18. Pickering, C. R. *et al.* Mutational landscape of aggressive cutaneous squamous cell
441 carcinoma. *Clin Cancer Res* **20**, 6582–92 (2014).
442 19. Stransky, N. *et al.* The mutational landscape of head and neck squamous cell carcinoma.
443 *Science* **333**, 1157–60 (2011).
444 20. The Cancer Genome Atlas. Comprehensive genomic characterization of squamous cell
445 lung cancers. *Nature* **489**, 519–25 (2012).
446 21. Cohen, E. E. W. *et al.* Pembrolizumab versus methotrexate, docetaxel, or cetuximab for
447 recurrent or metastatic head-and-neck squamous cell carcinoma (KEYNOTE-040): a
448 randomised, open-label, phase 3 study. *The Lancet* **393**, 156–167 (2019).
449 22. Chow, L. Q. M. Head and Neck Cancer. *New England Journal of Medicine* **382**, 60–72
450 (2020).
451 23. Hirano, H. & Kato, K. Systemic treatment of advanced esophageal squamous cell
452 carcinoma: Chemotherapy, molecular-targeting therapy and immunotherapy. *Jpn J Clin*
453 *Oncol* **49**, 412–420 (2019).
454 24. Kono, M., Saito, S., Egloff, A. M., Allen, C. T. & Uppaluri, R. The mouse oral carcinoma
455 (MOC) model: A 10-year retrospective on model development and head and neck cancer
456 investigations. *Oral Oncol* **132**, 106012 (2022).
457 25. Kim, E. M., Bae, Y. M., Choi, M. H. & Hong, S. T. Cyst formation, increased anti-
458 inflammatory cytokines and expression of chemokines support for Clonorchis sinensis
459 infection in FVB mice. *Parasitol Int* **61**, 124–129 (2012).

460 26. McCreery, M. Q. *et al.* Evolution of metastasis revealed by mutational landscapes of
461 chemically induced skin cancers. *Nat Med* **21**, 1514–1520 (2015).
462 27. Wong, C. E. *et al.* Inflammation and Hras signaling control epithelial-mesenchymal
463 transition during skin tumor progression. *Genes Dev* **27**, 670–82 (2013).
464 28. Reeves, M. Q., Kandyba, E., Harris, S., Del Rosario, R. & Balmain, A. Multicolour lineage
465 tracing reveals clonal dynamics of squamous carcinoma evolution from initiation to
466 metastasis. *Nat Cell Biol* **20**, 699–709 (2018).
467 29. Nassar, D., Latil, M., Boeckx, B., Lambrechts, D. & Blanpain, C. Genomic landscape of
468 carcinogen-induced and genetically induced mouse skin squamous cell carcinoma. *Nat*
469 *Med* **21**, 946–954 (2015).
470 30. Li, Y. R. *et al.* Long Term Latency of Highly Mutated Cells in Normal Mouse Skin is
471 Reversed by Exposure to Tumor Promoters and Chronic Tissue Damage. *Cancer Discov*
472 (2025).
473 31. DeVette, C. I. *et al.* NetH2pan: A computational tool to guide MHC peptide prediction on
474 murine tumors. *Cancer Immunol Res* **6**, 636–644 (2018).
475 32. Castle, J. C. *et al.* Exploiting the mutanome for tumor vaccination. *Cancer Res* **72**, 1081–
476 1091 (2012).
477 33. Alspach, E. *et al.* MHC-II neoantigens shape tumour immunity and response to
478 immunotherapy. *Nature* **574**, 696–701 (2019).
479 34. Matsushita, H. *et al.* Cancer exome analysis reveals a T-cell-dependent mechanism of
480 cancer immunoediting. *Nature* **482**, 400–404 (2012).

481 35. Yadav, M. *et al.* Predicting immunogenic tumour mutations by combining mass
482 spectrometry and exome sequencing. *Nature* **515**, 572–576 (2014).
483 36. DeVette, C. I. *et al.* A pipeline for identification and validation of tumor-specific antigens
484 in a mouse model of metastatic breast cancer. *Oncoimmunology* **9**, 1685300 (2020).
485 37. Tanaka, M. *et al.* Tumor cell heterogeneity drives spatial organization of the intratumoral
486 immune response. *J Exp Med* **222**, e20242282 (2025).
487 38. Martin, M. Cutadapt removes adapter sequences from high-throughput sequencing
488 reads. *EMBnet J* **17**, 10 (2011).
489 39. Li, H. & Durbin, R. Fast and accurate short read alignment with Burrows-Wheeler
490 transform. *Bioinformatics* **25**, 1754–60 (2009).
491 40. Van der Auwera, G. A. & O'Connor, B. D. *Genomics in the Cloud: Using Docker, GATK, and*
492 *WDL in Terra*. (O'Reilly Media, 2020).
493 41. Cibulskis, K. *et al.* Sensitive detection of somatic point mutations in impure and
494 heterogeneous cancer samples. *Nat Biotechnol* **31**, 213–9 (2013).
495 42. Kim, S. *et al.* Strelka2: fast and accurate calling of germline and somatic variants. *Nat*
496 *Methods* **15**, 591–594 (2018).
497 43. Wang, K., Li, M. & Hakonarson, H. ANNOVAR: functional annotation of genetic variants
498 from high-throughput sequencing data. *Nucleic Acids Res* **38**, e164 (2010).
499 44. Talevich, E., Shain, A. H. & Bastian, B. C. CNVkit: Copy number detection and
500 viziualization for targeted sequencing using off-target reads. *PLoS Comput Biol* **12**,
501 e1004873 (2016).
502

# Figure 1

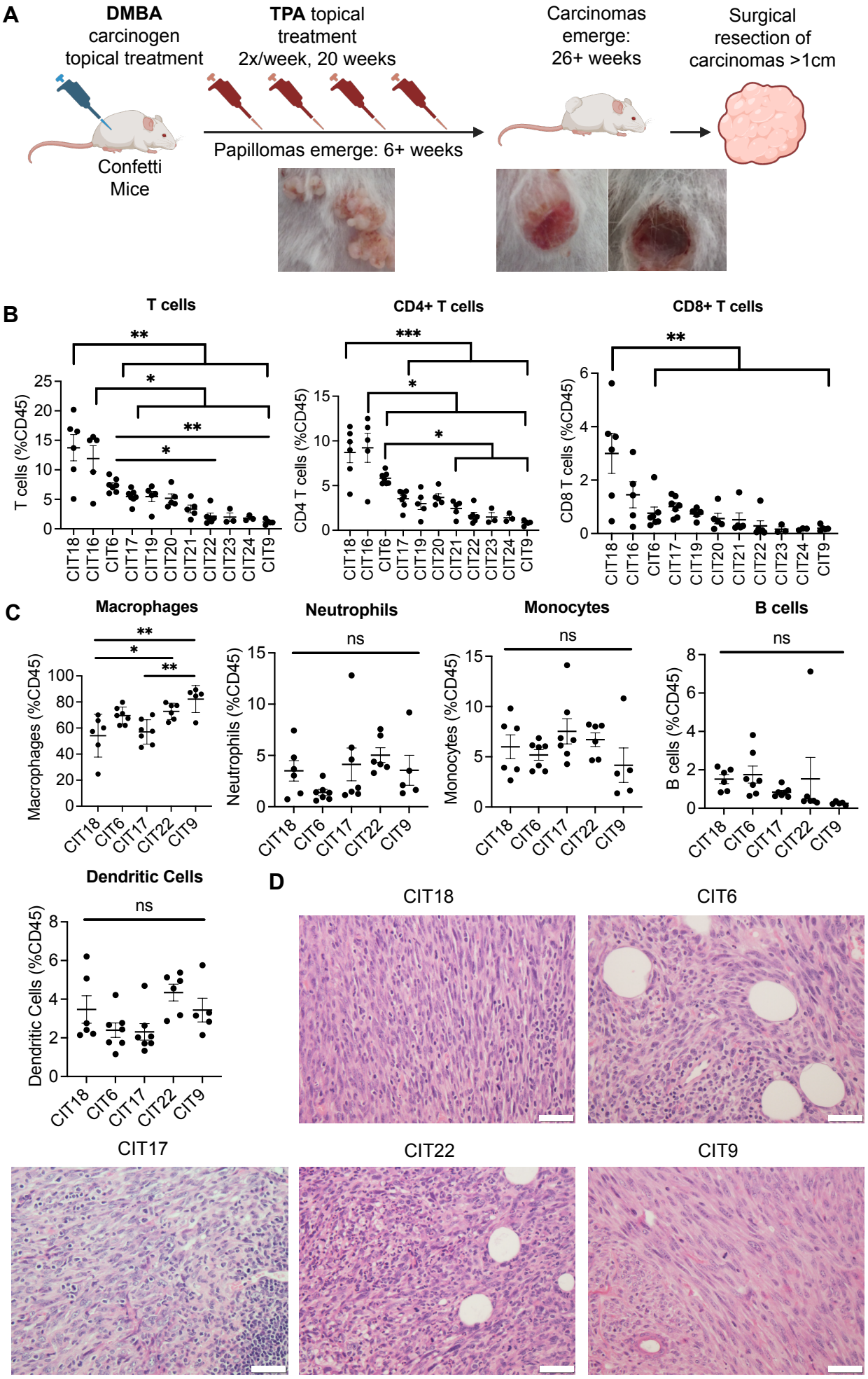
A
DMBA carcinogen topical treatment
Confetti Mice
TPA topical treatment 2x/week, 20 weeks
Papillomas emerge: 6+ weeks
Carcinomas emerge: 26+ weeks
Surgical resection of carcinomas >1cm
B
T cells
T cells (%CD45)
CD4+ T cells
CD4 T cells (%CD45)
CD8+ T cells
CD8 T cells (%CD45)
CIT18 CIT16 CIT6 CIT17 CIT19 CIT20 CIT21 CIT22 CIT23 CIT24 CIT9
C
Macrophages
Macrophages (%CD45)
Neutrophils
Neutrophils (%CD45)
Monocytes
Monocytes (%CD45)
B cells
B cells (%CD45)
ns
CIT18 CIT6 CIT17 CIT22 CIT9
Dendritic Cells
Dendritic Cells (%CD45)
D
CIT18
CIT6
CIT17
CIT22
CIT9

504 **Figure 1. Immune infiltration and histology profiles of CIT lines.**

505 **(A)** Schematic of CIT cell line generation. Tumors were induced with the DMBA/TPA

506 carcinogenesis model, and cell lines were established from malignant carcinomas. **(B)**

507 Quantification of total T cells, CD4+ T cells and CD8+ T cells by flow cytometry in each CIT line.

508 **(C)** Quantification of macrophages, neutrophils, monocytes, B cells and dendritic cells by flow

509 cytometry in 5 selected CIT lines. **(D)** Representative images of tumors from selected CIT lines

510 stained with hematoxylin and eosin (H&E) for histological analysis. Scale bar = 20 μm. Statistical

511 analysis in (B-C) by one-way ANOVA with Tukey post-hoc test. * $p < 0.05$, ** $p < 0.01$, *** $p <$

512 0.001.

513

514

# Figure 2

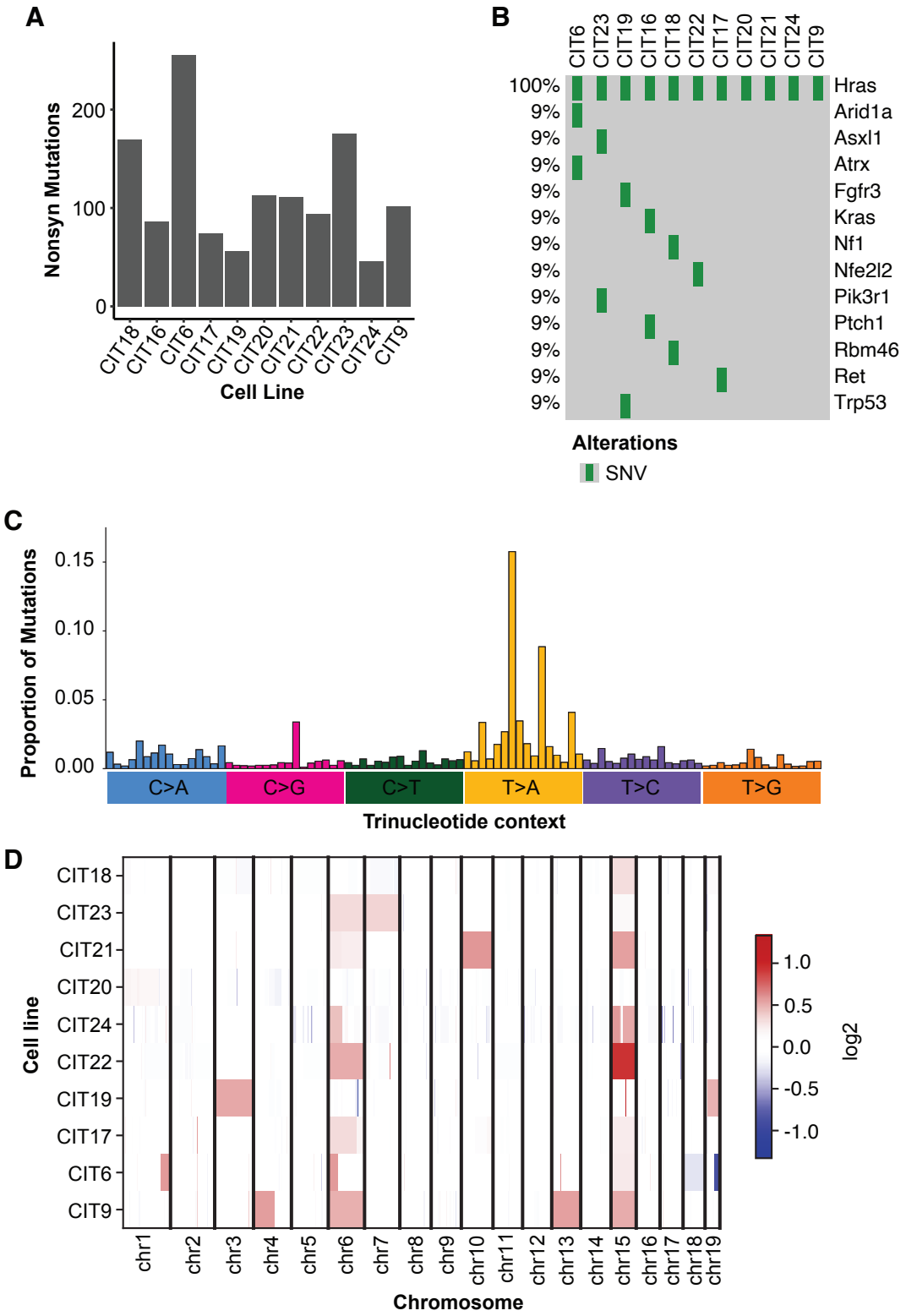
A
Nonsyn Mutations
200
100
0
CIT18
CIT16
CIT6
CIT17
CIT19
CIT20
CIT21
CIT22
CIT23
CIT24
CIT9
Cell Line
B
CIT6
CIT23
CIT19
CIT16
CIT18
CIT22
CIT17
CIT20
CIT21
CIT24
CIT9
100% Hras
9% Arid1a
9% Asxl1
9% Atrx
9% Fgfr3
9% Kras
9% Nf1
9% Nfe2l2
9% Pik3r1
9% Ptch1
9% Rbm46
9% Ret
9% Trp53
Alterations
SNV
C
Proportion of Mutations
0.15
0.10
0.05
0.00
C>A
C>G
C>T
T>A
T>C
T>G
Trinucleotide context
D
Cell line
CIT18
CIT23
CIT21
CIT20
CIT24
CIT22
CIT19
CIT17
CIT6
CIT9
chr1
chr2
chr3
chr4
chr5
chr6
chr7
chr8
chr9
chr10
chr11
chr12
chr13
chr14
chr15
chr16
chr17
chr18
chr19
Chromosome
1.0
0.5
0.0
-0.5
-1.0
log2

515 **Figure 2. Genetic profiling of CIT lines.**

516 **(A)** Number of non-synonymous mutations per cell line, based on exome sequencing. **(B)** Genes
517 mutated in CIT lines which are known to be commonly mutated in human SCC. **(C)** Frequencies
518 of mutations observed in each of 96 possible trinucleotide contexts for all mutations in CIT cell
519 lines. Trinucleotide contexts, arranged on the x axis, are grouped by the base pair change of the
520 mutation. Highest peaks are observed at CTG>A and GTG>A. **(D)** CNV alterations detected in
521 each chromosome in CIT lines based on exome sequencing. Red denotes copy number gains,
522 blue denotes copy number losses.

523

524

# Figure 3

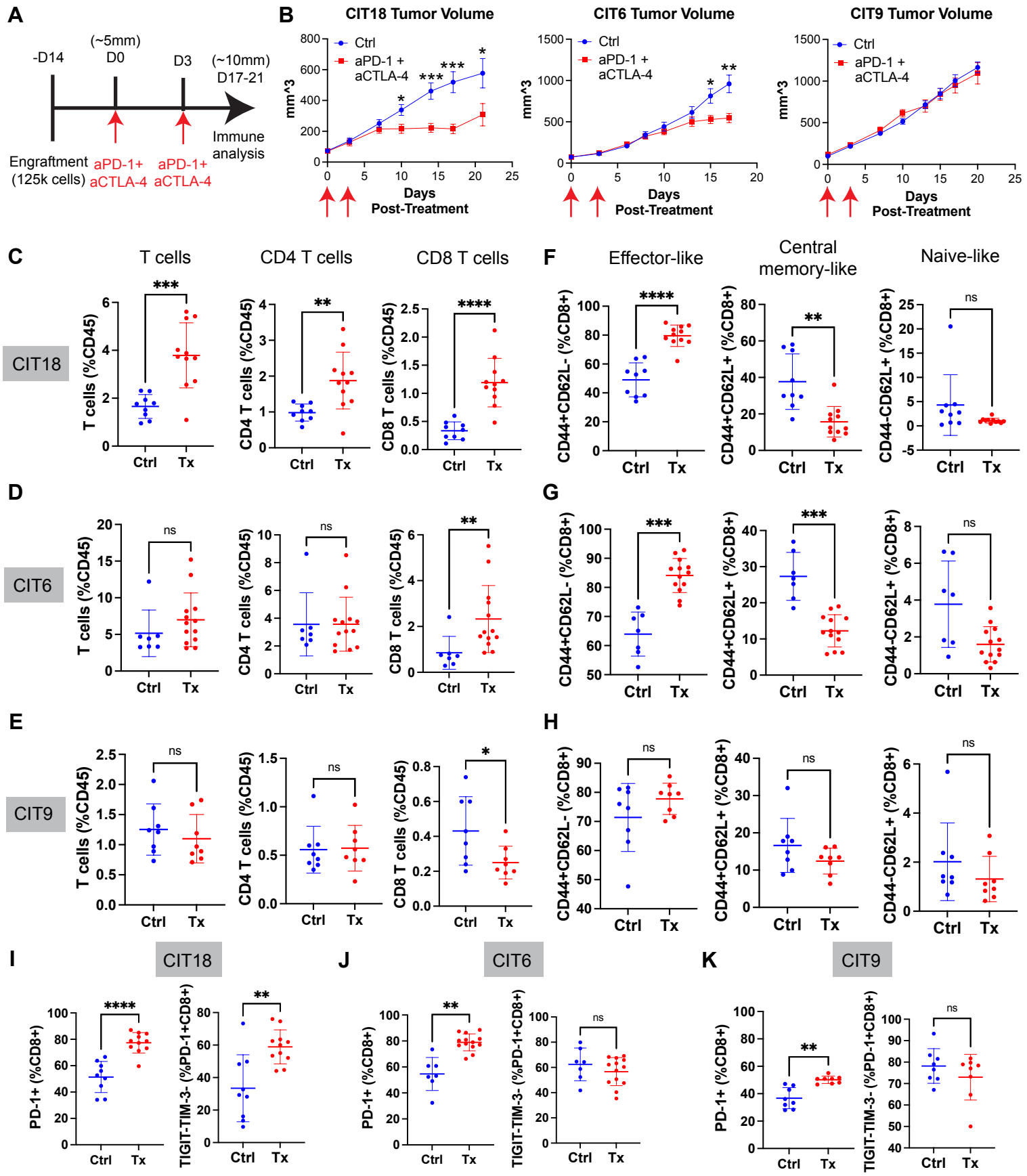
A
-D14
(~5mm)
D0
D3
(~10mm)
D17-21
Engraftment
(125k cells)
aPD-1+
aCTLA-4
aPD-1+
aCTLA-4
Immune
analysis
B
CIT18 Tumor Volume
CIT6 Tumor Volume
CIT9 Tumor Volume
Ctrl
aPD-1 +
aCTLA-4
mm^3
Days
Post-Treatment
C
T cells
CD4 T cells
CD8 T cells
CIT18
T cells (%CD45)
CD4 T cells (%CD45)
CD8 T cells (%CD45)
Ctrl
Tx
D
CIT6
E
CIT9
F
Effector-like
Central
memory-like
Naive-like
CD44+CD62L- (%CD8+)
CD44+CD62L+ (%CD8+)
CD44-CD62L+ (%CD8+)
G
H
I
CIT18
PD-1+ (%CD8+)
TIGIT-TIM-3- (%PD-1+CD8+)
J
CIT6
K
CIT9
ns

525 **Figure 3. Immunologically hot CIT lines are responsive to combined anti-PD-1 and anti-CTLA-4**
526 **immune checkpoint inhibitor (ICI) therapy.**
527 **(A)** Schematic of ICI treatment regimen on CIT tumor-bearing mice. **(B)** Average tumor volumes
528 of immunologically hot CIT18 and CIT6 tumors and immunologically cold CIT9 tumors after
529 combined ICI therapy, compared to tumors treated with isotype control antibodies. **(C-E)** Total
530 T cell, CD4+ T cell, and CD8+ T cell infiltration of CIT18 (C), CIT6 (D) and CIT9 (E) tumors as a
531 percentage of all CD45+ immune cells. **(F-H)** Abundance of effector subsets of CD8+ T cells
532 defined by the combinatorial expressions of CD44 and CD62L in CIT18 (F), CIT6 (G) and CIT9 (H)
533 tumors. **(I-K)** Abundance of CD8+ T cells expressing PD-1, and frequency of "activated" PD-
534 1+Tim3-TIGIT- CD8+ T cells in CIT18 (I), CIT6 (J) and CIT9 (K) tumors. All statistical analyses
535 performed with Welch's t-test. * $p < 0.05$, ** $p < 0.01$, *** $p < 0.001$, **** $p < 0.001$.
536
537

# Figure 4

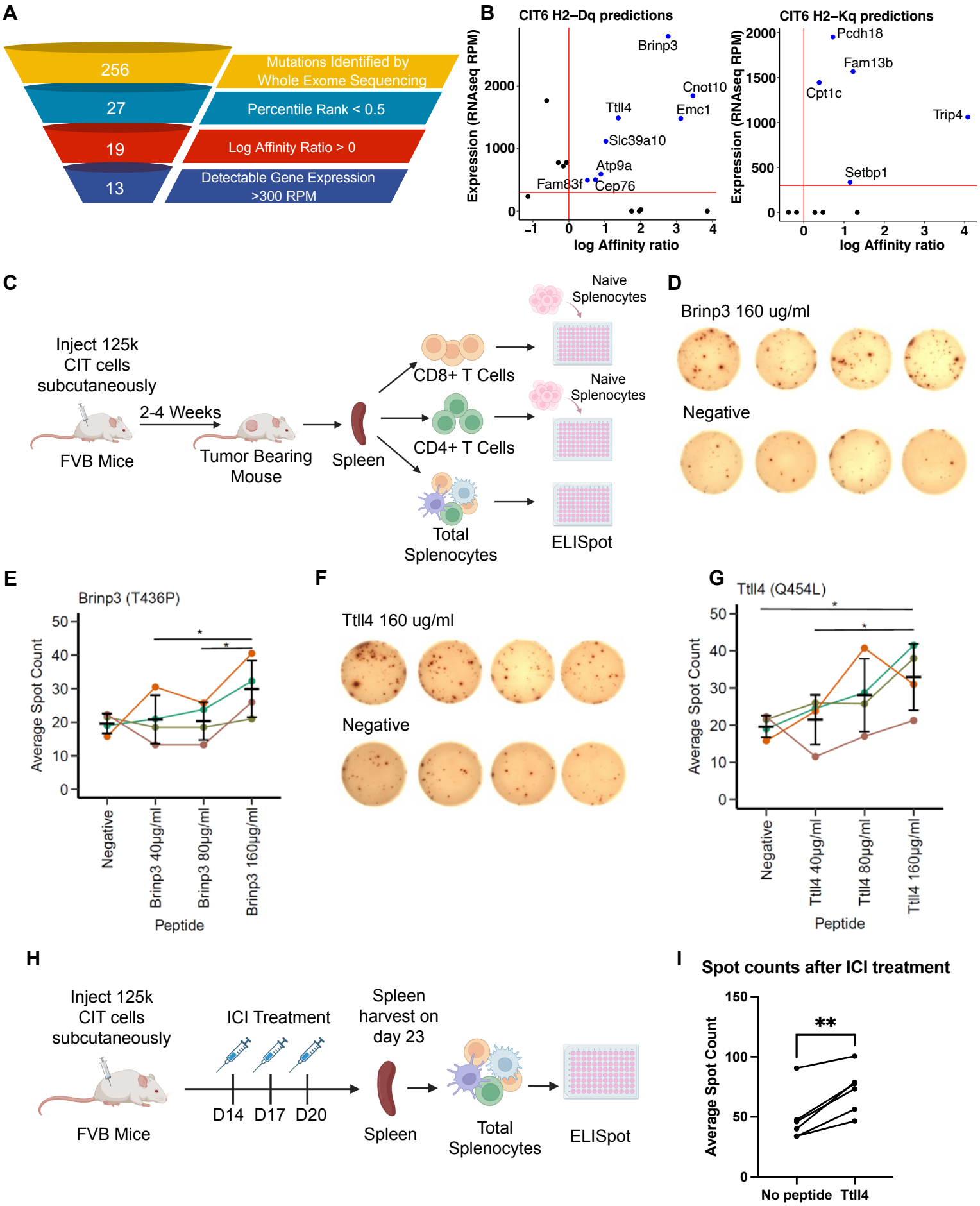
A
256
Mutations Identified by Whole Exome Sequencing
27
Percentile Rank < 0.5
19
Log Affinity Ratio > 0
13
Detectable Gene Expression >300 RPM
B
CIT6 H2–Dq predictions
Expression (RNAseq RPM)
log Affinity ratio
Brinp3
Cnot10
Ttll4
Emc1
Slc39a10
Atp9a
Fam83f
Cep76
CIT6 H2–Kq predictions
Pcdh18
Fam13b
Cpt1c
Trip4
Setbp1
C
Inject 125k CIT cells subcutaneously
FVB Mice
2-4 Weeks
Tumor Bearing Mouse
Spleen
CD8+ T Cells
CD4+ T Cells
Total Splenocytes
Naive Splenocytes
ELISpot
D
Brinp3 160 ug/ml
Negative
E
Brinp3 (T436P)
Average Spot Count
Negative
Brinp3 40µg/ml
Brinp3 80µg/ml
Brinp3 160µg/ml
Peptide
F
Ttll4 160 ug/ml
Negative
G
Ttll4 (Q454L)
Average Spot Count
Negative
Ttll4 40µg/ml
Ttll4 80µg/ml
Ttll4 160µg/ml
Peptide
H
Inject 125k CIT cells subcutaneously
FVB Mice
ICI Treatment
D14 D17 D20
Spleen harvest on day 23
Spleen
Total Splenocytes
ELISpot
I
Spot counts after ICI treatment
Average Spot Count
No peptide
Ttll4

538 **Figure 4. CIT lines express identifiable neoantigens whose cognate CD8+ T cells are responsive**
539 **to immunotherapy.**
540 **(A)** Selection criteria for CIT6 mutations predicted to generate neoantigens. **(B)** Predicted
541 peptide log affinity ratio (affinity ratio is defined as ratio between predicted binding affinity of
542 mutant versus wild-type sequence) and gene expression level of mutations predicted to be top
543 CIT6 candidate neoantigens, shown for H2-Dq and H2-Kq alleles. Affinity predictions were
544 generated using NetH2Pan algorithm. **(C)** Schematic of IFNγ ELISpot assay. For screening of
545 CD8+ T cell and CD4+ T cell responses, CD8+ or CD4+ T cells were isolated from the spleens of
546 tumor bearing mice and co-cultured with total splenoyctes from a healthy tumor-naïve mouse.
547 **(D)** Representative IFNγ ELISpot images of assay peformed with CD8+ T cells from the spleen of
548 CIT6-bearing mice cultured with 160ug/ml of Brinp3 peptide CPAFLPCTV (top row) and negative
549 control (no peptide, bottom row). **(E)** Quantification of average IFNγ ELISpot spot counts for
550 CD8+ T cells from the spleen of CIT6-bearing mice cultured with different concentrations of
551 Brinp3 peptide CPAFLPCTV. Each colored line represents data points from a different mouse.
552 **(F)** Representative IFNγ ELISpot images of assay peformed with CD8+ T cells from the spleen of
553 CIT6-bearing mice cultured with 160ug/ml of Ttll4 peptide VPPSSLLPL (top row) and negative
554 control (no peptide, bottom row). **(G)** Quantification of average IFNγ ELISpot spot counts for
555 CD8+ T cells from the spleen of CIT6-bearing mice cultured with different concentrations of
556 Ttll4 peptide VPPSSLLPL. **(H)** Schematic of immune checkpoint inhibitor (ICI) treatment regimen
557 and ELISpot analysis. **(I)** Average spot counts of ICI-treated splenocytes cultured with 80ug/ml
558 of Ttll4 peptide vs negative control. Statistical analysis in panels E, G, and I was done by paired
559 t-test. * $p < 0.05$, ** $p < 0.01$.

# Supplemental Figure 1

**A**

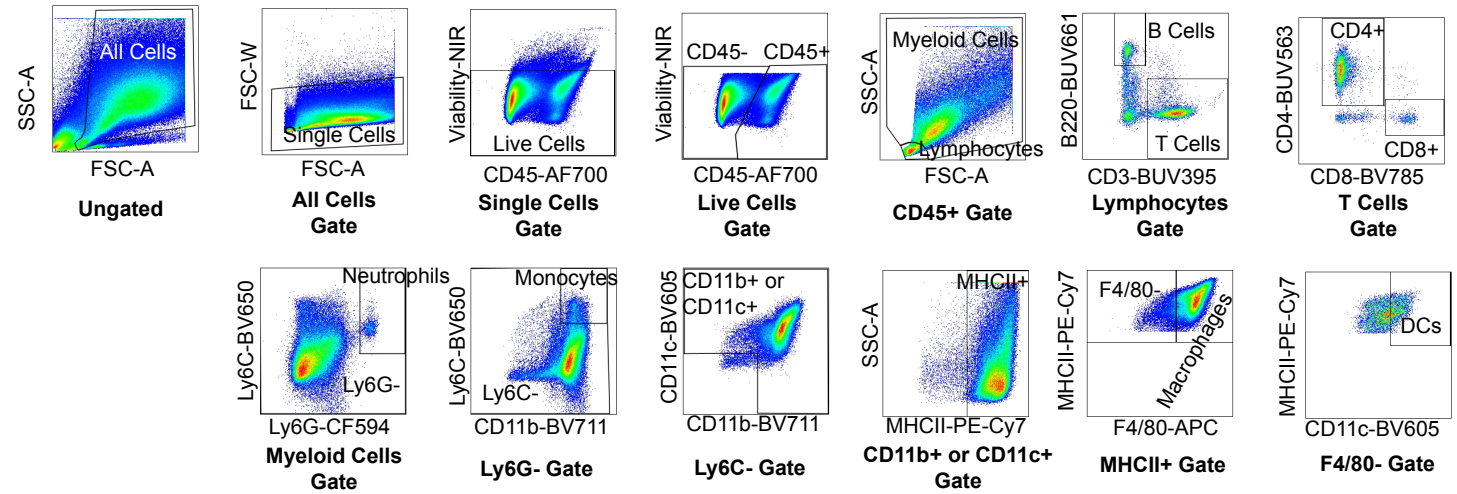


**B**

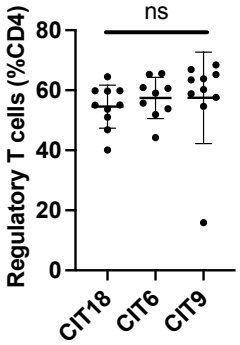

560 **Supp. Fig 1. Flow cytometry gating strategy and regulatory T cell infiltration in CIT tumors.**

561 **(A**) Flow cytometric gating strategy of main immune cell types. Immune analysis of a CIT6

562 tumor is shown as representative data. **(B)** Abundance of Foxp3+CD25+ regulatory T cells

563 (Tregs) as percentage of CD4+ T cells in CIT18, CIT6 and CIT9 tumors. Statistical analysis by One-

564 way ANOVA with Tukey post-hoc test.

565

566

# Supplemental Figure 2

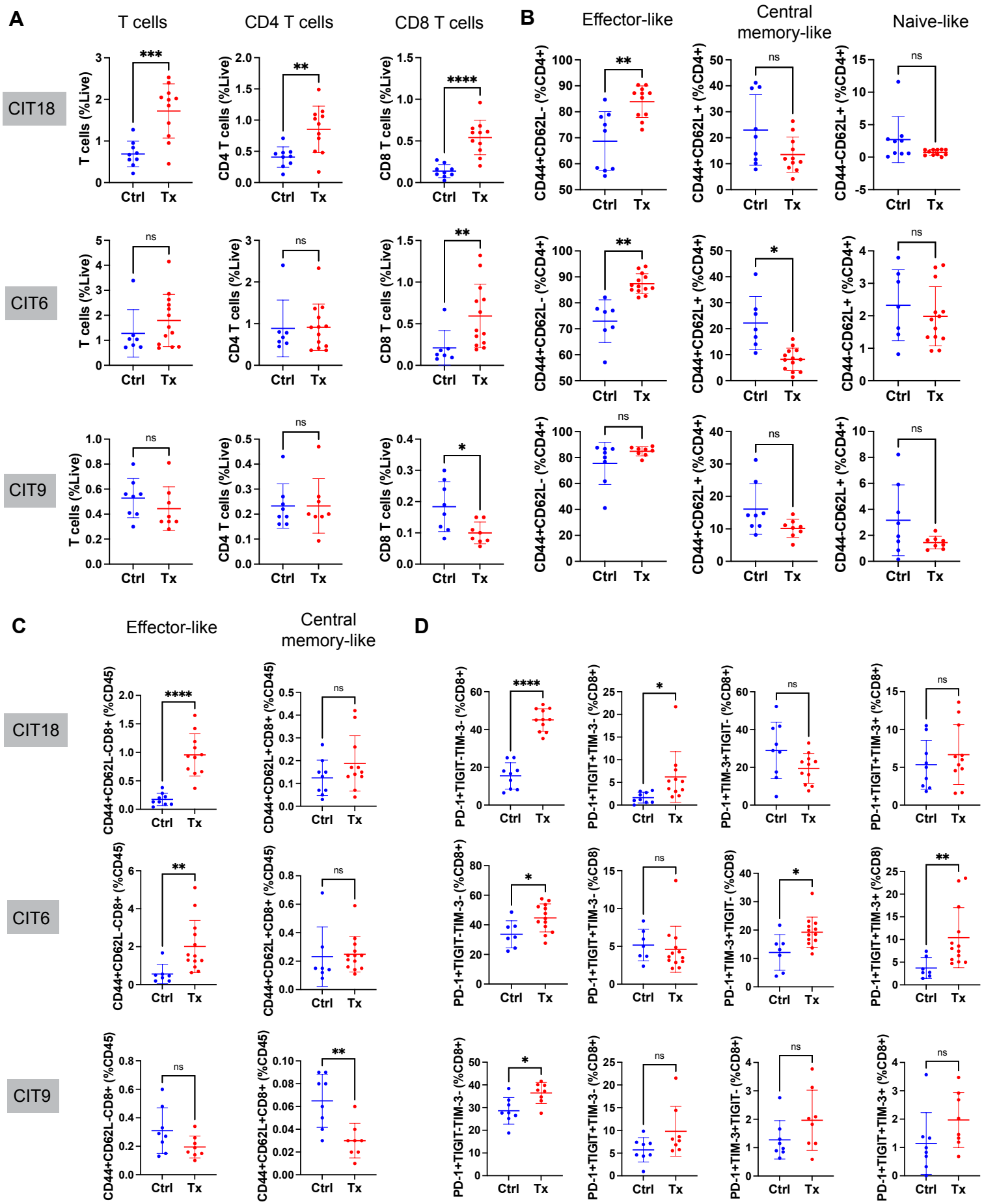

567 **Supp. Fig. 2. Tumor-infiltrating T cell effector activity after treatment with combined anti-PD-**

568 **1 and anti-CTLA-4 immune checkpoint inhibitor (ICI) therapy.**

569 **(A)** Total T cell, CD4+ T cell, and CD8+ T cell infiltration of CIT18, CIT6 and CIT9 as percentage of

570 all live cells, including tumor and stromal cells. **(B)** Abundance of effector subsets of CD4+ T

571 cells defined by the combinatorial expressions of CD44 and CD62L in CIT18, CIT6 and CIT9. **(C)**

572 Infiltration of CD44+CD62L- "effector-like" CD8+ T cells and CD44+CD62L+ "central memory-

573 like" CD8+ T cells as percentage of all CD45+ immune cells. **(D)** Abundance of CD8+ PD-1+ T cells

574 expressing specific combinations of TIGIT and Tim3 exhaustion markers in CIT18, CIT6 and CIT9

575 tumors. All statistical analyses performed with Welch's t-test. * $p < 0.05$, ** $p < 0.01$, *** $p <$

576 $0.001$, **** $p < 0.001$.

577

578

# Supplemental Figure 3

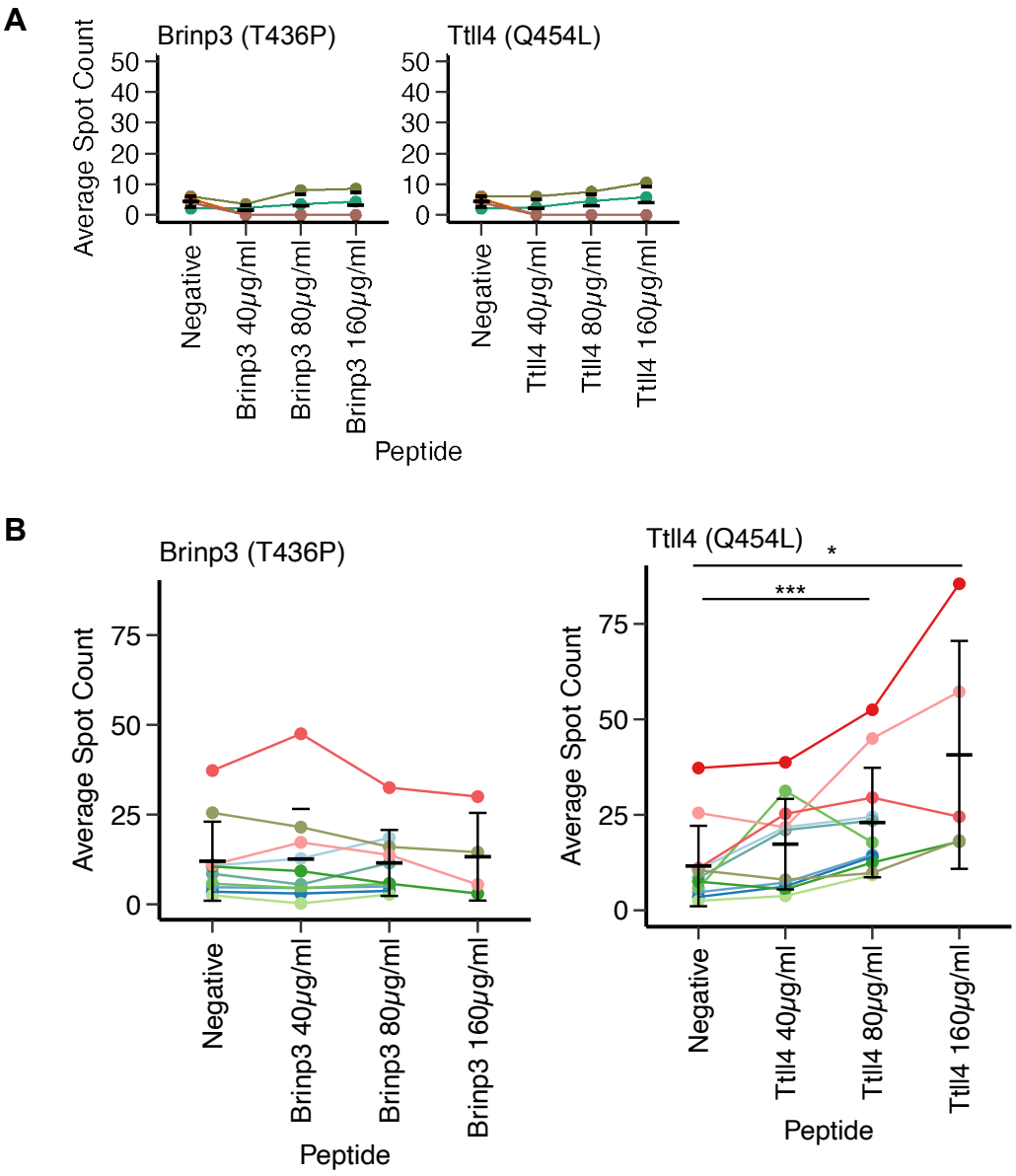

579 **Supp. Fig. 3. CIT6 ELISpot analysis of unfractionated splenocytes and CD4+ splenocytes.**

580 **(A)** Spot counts from ELISpot assays performed with CD4+ T cells isolated from the spleens of

581 CIT6-bearing mice and cultured with splenocytes from tumor-naïve mice loaded with increasing

582 concentrations of Brinp3 and Ttll4 peptides. **(B)** Spot counts from ELISpot assays performed

583 with total splenocytes from CIT6-bearing mice cultured with increasing concentrations of

584 Brinp3 and Ttll4 peptides. All statistical analyses performed with paired t-test. * $p < 0.05$, ** $p <$

585 $0.01$, *** $p < 0.001$.

586

587

| **Table 1**: Number of Non-Synonymous Mutations per CIT Cell Line | |
|---|---|
| **Cell Line** | **Non-Synonymous Mutations** |
| CIT18 | 170 |
| CIT16 | 86 |
| CIT6 | 256 |
| CIT17 | 74 |
| CIT19 | 56 |
| CIT20 | 113 |
| CIT21 | 111 |
| CIT22 | 94 |
| CIT23 | 176 |
| CIT24 | 46 |
| CIT9 | 102 |

588 **Table 1: Number of non-synonymous mutations per CIT cell line.** Number of non-synonymous

589 mutations based on exome sequencing of CIT cell lines.

590

591

| **Table 2**: List of Filtered Peptide Candidates for CIT6 Antigens | | | | |
|---|---|---|---|---|
| **Gene** | **Amino Acid Change** | **Peptide** | **Allele** | **Percentile Rank** |
| Slc39a10 | S286I | LPEHIGHEL | Dq | 0.0225 |
| Ttll4 | Q454L | VPPSSLLPL | Dq | 0.1367 |
| Brinp3 | T436P | CPAFLPCTV | Dq | 0.2119 |
| Cep76 | P158A | VPCACEADF | Dq | 0.4240 |
| Atp9a | I216F | EPNIDFHNF | Dq | 0.4662 |
| Fam83f | Q4L | VPALPTESL | Dq | 0.1392 |
| Emc1 | H307L | SHYALLHYL | Dq | 0.2106 |
| Cnot10 | A543P | VPLALGDNL | Dq | 0.0063 |
| Fam13b | D766H | QEKLARHL | Kq | 0.1266 |
| Setbp1 | N1160Y | HDYLSGLF | Kq | 0.2688 |
| Pcdh18 | M631I | NEENIFII | Kq | 0.1341 |
| Cpt1c | Q29H | HEIYLCAL | Kq | 0.3203 |
| Trip4 | Q423L | HQHQLRIL | Kq | 0.3234 |

592 **Table 2: List of filtered peptide candidates for CIT6 neoantigens.** List of all neoantigen peptide

593 candidates that met the criteria specified in Fig. 4A. Percentile ranked based on NetH2pan

594 algorithm.

595

596

**Table 3**: List of Antibodies and Conjugated Fluorophores used for Flow Cytometry Analysis

| Target | Fluorophore | Clone | Dilution | Manufacturer | Catalog # |
|---|---|---|---|---|---|
| B220 | BUV661 | RA3-6B2 | 1:200 | BD Biosciences | 612972 |
| CD11b | BV711 | M1/70 | 1:100 | BioLegend | 101242 |
| CD11c | BV605 | N418 | 1:100 | BioLegend | 117334 |
| CD16/CD32 (FcR Block) | N/A | 2.4G2 | 1:167 | Tonbo | 70-0161-U500 |
| CD3e | BUV395 | 145-2C11 | 1:62.5 | BD Biosciences | 563565 |
| CD4 | BUV563 | GK1.5 | 1:200 | BD Biosciences | 612923 |
| CD44 | BV785 | 1M7 | 1:200 | BioLegend | 103059 |
| CD45 | AlexaFluor700 | 30-F11 | 1:400 | BioLegend | 103128 |
| CD62L | FITC | MEL-14 | 1:200 | Invitrogen | 11-0621-81 |
| CD8a | BV570 | 53-6.7 | 1:200 | BioLegend | 100739 |
| CD8a | BV785 | 53-6.7 | 1:200 | BioLegend | 100750 |
| F4/80 | APC | BM8 | 1:100 | BioLegend | 123116 |
| FoxP3 | PE-Cy7 | FJK-16s | 1:50 | eBioscience | 25-5773-82 |
| Live/Dead | NIR | N/A | 1:1000 | Invitrogen | L34976A |
| Ly6C | BV650 | HK1.4 | 1:200 | BioLegend | 128049 |
| Ly6G | PE-CF594 | 1A8 | 1:200 | BD Biosciences | 562700 |
| MHCII | PE-Cy7 | M5/114.15.2 | 1:400 | BioLegend | 107630 |
| PD-1 | BV605 | 29F.1A12 | 1:100 | BD Biosciences | 135220 |
| TIGIT | BV421 | 1G9 | 1:100 | BioLegend | 142111 |
| Tim3 | APC | RMT3-23 | 1:100 | BioLegend | 119705 |

597 **Table 3: List of antibodies used for flow cytometry analysis.** All antibodies, clone number, and

598 conjugated fluorophores for antibodies used for flow cytometry.

599

600